Journal of Sound and Vibration (1999) **224**(5), 843–862
Article No. jsvi.1999.2164, available online at http://www.idealibrary.com on IDEAL®

LAMB WAVE SCATTERING FROM A THROUGH HOLE

J. C. P. McKeon
Sonix Inc., 8700 *Morrissette Drive*, *Springfield*, *VA* 22152, *U.S.A*.
AND
M. K. Hinders
College of William and Mary, *Department of Applied Science*, *Williamsburg*, *VA* 23187, *U.S.A*.

(*Received* 1 *September* 1998, *and in final form* 5 *February* 1999)

Ultrasonic guided waves, Lamb waves, are useful for evaluating the integrity of plate and shell structures common in many applications. Tomographic reconstruction with Lamb waves allows for the accurate reconstruction of the variation of quantities of interest throughout the investigated region, and it presents the data as a quantitative map. The location, shape, and extent of flaws can then be easily extracted from this tomographic image. The scattering of Lamb waves from severe flaws introduces artifacts in such reconstructions, however. In this paper higher order plate theory is used to derive analytical solutions for the scattering of the lowest order symmetric Lamb waves from a circular inclusion, focusing in particular on isolated through holes in plates. Plane wave and point source scattering behavior is explored for holes of different diameters, and a finite-beam solution is constructed by superposition of point source solutions. These results are then used to explain the scattering effects seen in Lamb wave contact scanning tomographic reconstructions.

1. INTRODUCTION

Lamb wave ultrasonics has become a standard technique for detecting corrosion, disbonds and cracks in metallic plates as well as fatigue and thermal damage in advanced composites [1–9]. More recently, a number of researchers have used tomographic reconstruction techniques to dramatically improve the usefulness of Lamb waves for quantitative non-destructive evaluation [10–16]. A Lamb wave contact scanning system has been developed that can perform tomographic reconstruction in both parallel projection and cross borehole configurations [17–19]. The reconstructions are sufficiently accurate that one is often limited by the simplifying assumptions in the Lamb wave models. In particular, the Lamb waves have been assumed to propagate along straight rays without diffraction or ray bending. This has allowed one to reconstruct the size, shape and depth of

0022–460X/99/300843 + 20 $30.00/0

thinned regions in plates, since a *small* change in thickness causes the velocity to change without scattering. For through holes, however, scattering of the Lamb waves is important. Figure 1 shows parallel projection tomographic reconstructions using the authors' Lamb wave scanner for through holes in aluminum plates. In the top image the hole is 5/8 in in diameter, which is smaller than the beam size so the hole is reproduced fairly accurately. The bottom image is a 1 in diameter hole, and because it is larger than the beam size, scattering effects are apparent. In particular, note the scalloped edge of the hole and the characteristic starburst pattern emanating from it.

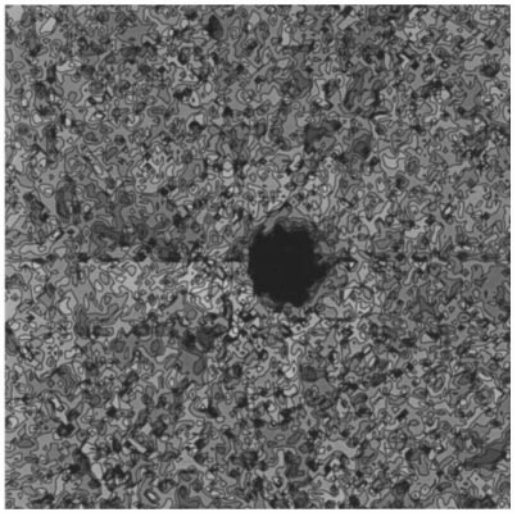

(a)

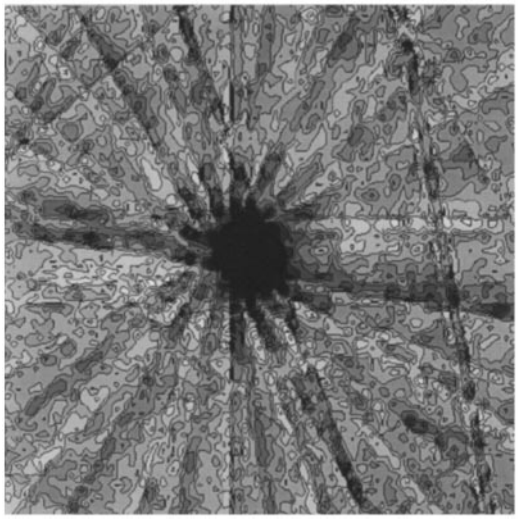

(b)

Figure 1. Parallel projection Lamb wave contact scanning tomographic reconstructions of (a) small and (b) large through holes in thin aluminum plates. Note the scalloped edge and the radial streaking pattern in (b) which are thought to be due to scattering effects.

Although diffraction tomography is well established in seismology, Lamb waves are guided waves for which scattering theories are not well developed [20–25]. In this paper Mindlin's higher-order plate theory [26–29] is adapted to model the scattering of the lowest order symmetric (S0) Lamb waves. The analysis here is similar to that done in reference [30] for the scattering of antisymmetric Lamb waves. The simplest plate theories only describe the dispersionless region of the $S0$ curve, but in the present measurements one makes use of the dispersion of the $S0$ wave so a theory that more accurately models the behavior of the $S0$ Lamb wave is needed. One first shows that the approximate Mindlin theory is valid over the frequency range of interest in the present experiments. Next, using this theory, analytical expressions for the scattering of $S0$ Lamb waves from a cylindrical inclusion in a plate are derived for an incident plane wave, a point source and a finite-area source. The expressions are explicitly evaluated for the case of a hole in a plate, and plots of the scattering behavior are used to explain the scattering effects seen in the images of Figure 1. One shows for the configuration used to acquire the data for Figure 1 that the presence of scattering effects are indeed important. The merits of this modelling approach in the development of Lamb wave diffraction tomography are also discussed.

2. THEORY OF KANE AND MINDLIN

Consider a thin homogeneous, isotropic, and linearly elastic plate lying in the xy-plane bounded by air at the planes $z = \pm h$. Because the thickness is small, the components of displacement for dilatational plate waves can be approximated by

$$u_x = v_x(x, y, t), \quad u_y = v_y(x, y, t), \quad u_z = (z/h)v_z(x, y, t), \tag{1}$$

where v_x, v_y, v_z are not functions of z. These can be expressed in terms of three independent scalar potentials, $\phi_1(x, y)$, $\phi_2(x, y)$, $\Psi(x, y)$ as

$$v_x = \left(\frac{\partial \phi_1}{\partial x} + \frac{\partial \phi_2}{\partial x} + \frac{\partial \Psi}{\partial y}\right)e^{-i\omega t}, \quad v_y = \left(\frac{\partial \phi_1}{\partial y} + \frac{\partial \phi_2}{\partial y} + \frac{\partial \Psi}{\partial x}\right)e^{-i\omega t},$$

$$v_z = (\sigma_1 \phi_1 + \sigma_2 \phi_2)e^{-i\omega t}, \tag{2}$$

which are chosen to satisfy the scalar Helmholtz equations

$$(\nabla^2 + k_1^2)\phi_1 = 0, \quad (\nabla^2 + k_2^2)\phi_2 = 0, \quad (\nabla^2 + K^2)\Psi = 0. \tag{3}$$

Here ∇^2 is the 2-D Laplacian, and the effective wavenumbers are given by

$$k_i^2 = (3\kappa^2/2\beta h)[(\alpha + \beta)\omega^2/\omega_0^2 - 1 - (-1)^i \psi], \quad i = 1, 2,$$

$$K^2 = \omega^2/c_T^2, \quad \sigma_i = \frac{h(\lambda + 2\mu)}{\kappa\lambda}\left(k_i^2 - \frac{\omega^2}{c_L^2}\right), \quad i = 1, 2,$$

$$\psi = [((\alpha+\beta)\omega^2/\omega_0^2 - 1)^2 + 4\alpha\beta(\omega^2/\omega_0^2)(1-\omega^2/\omega_0^2)]^{1/2},$$

$$\alpha = c_L^2/c_P^2, \quad \beta = c_T^2/c_P^2, \quad \omega_0^2 = \pi^2(\lambda+2\mu)/4h^2\rho,$$

$$c_L^2 = (\lambda+2\mu)/\rho, \quad c_T^2 = \mu/\rho, \quad c_P^2 = 4\mu(\lambda+\mu)/\rho(\lambda+2\mu).$$

In these equations, ρ is the mass density, λ and μ are the Lamé parameters, and c_L, c_T and c_P are the compressional, shear, and plate wave speeds in isotropic media. Also, ω_0 is the frequency corresponding to the first mode of pure thickness vibration of an infinite plate, and the parameter $\kappa^2 = \pi^2/12$ is inserted *ad hoc* to improve the results.

If any one of the functions ϕ_1, ϕ_2, or Ψ is taken to be proportional to $e^{i\gamma x}$ while the remaining two are set equal to zero, there results a plane wave propagating in the x direction and having a wavelength and velocity equal to $2\pi/\gamma$ and ω/γ respectively. In order to satisfy the above conditions, $\gamma = k_1$, k_2, or K depending on which potential is non-zero.

To compare this plate theory with the exact theory, the phase velocity, c, is considered. For $\phi_i \neq 0$, $i = 1, 2$, $\Psi = 0$,

$$c = (2\alpha c_T^2\omega^2/\omega_0^2[(\alpha-\beta)\omega^2/\omega_0^2 - 1 - (-1)^i\psi]^{-1})^{1/2} \tag{4}$$

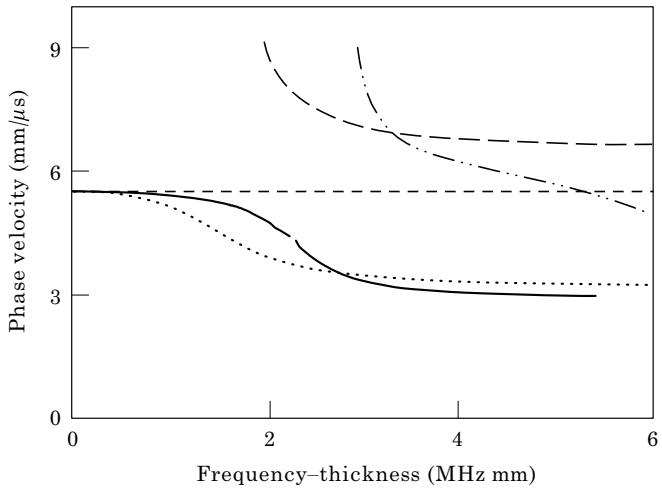

Figure 2. Dispersion curves of the exact Rayleigh–Lamb theory for the two lowest order symmetric modes compared to approximate Mindlin theory and simple plate theory. The solid line is the exact $S0$ curve and the dotted line is the corresponding Mindlin theory for that mode. The straight dashed line is the simple dispersionless theory for this extensional mode. The straight dashed line is the simple dispersionless theory for this extensional mode. The dot-dot dash line is the exact $S1$ mode and the long dash is the corresponding mode from the Mindlin theory.

and for $\phi_i = 0$, $i = 1, 2$, $\Psi \neq 0$,

$$c = c_T. \tag{5}$$

Equation (5) obviously shows that the $\Psi \neq 0$ wave matches the shear horizontal wave of the exact theory. However, in order to verify these expressions for the $S0$ ($i = 1$) and $S1$ ($i = 2$) Lamb waves, plots of these expressions for phase velocity versus "frequency–thickness" can be examined. Figure 2 shows the two lowest order symmetric ($S0$ and $S1$) Rayleigh–Lamb dispersion curves for an aluminum plate, as well as the corresponding dispersion curves using the Mindlin theory. Notice that the present theory is in qualitative agreement with the exact theory over the full range of frequency–thickness shown. Most importantly, the dispersion behavior of the $S0$ and $S1$ modes has been captured by the higher order plate theory. The simple plate theory (also shown) does not model the dispersion behavior of the $S0$ mode, while the full three-dimensional theory is too complicated to use for scattering calculations. These two-dimensional higher-order plate theory expressions for the $S0$ and $S1$ Lamb wave modes contain enough of the mathematical complexity of the symmetric Lamb waves to model that part of their behavior which is employed in the measurement, but are not too complicated to prevent their use in analytical scattering analysis.

3. SCATTERING FROM CYLINDRICAL INCLUSIONS

One next considers the infinite plate with an in-plane disk of radius $r = a$ and semithickness h', at the origin of a cylindrical co-ordinate system. The disk has material parameters (ρ', λ', μ') that are arbitrarily different from those of the plate (ρ, λ, μ).

For thin plates one assumes that the components of displacement in cylindrical co-ordinates are approximated sufficiently well by

$$u_r(r, \theta, t) = v_r(r, \theta, t), \quad u_\theta(r, \theta, t) = v_\theta(r, \theta, t), \quad u_z(r, \theta, t) = (z/h)v_z(r, \theta, t). \tag{6}$$

Introducing three independent displacement potentials $\phi_1(r, \theta)$, $\phi_2(r, \theta)$, $\Psi(r, \theta)$ allows one to write the displacement components as

$$v_r = \left(\frac{\partial \phi_1}{\partial r} + \frac{\partial \phi_2}{\partial r} + \frac{1}{r}\frac{\partial \Psi}{\partial \theta}\right)e^{-i\omega t}, \quad v_\theta = \left(\frac{1}{r}\frac{\partial \phi_1}{\partial \theta} + \frac{1}{r}\frac{\partial \phi_2}{\partial \theta} - \frac{\partial \Psi}{\partial r}\right)e^{-i\omega t},$$
$$v_z = (\sigma_1 \phi_1 + \sigma_2 \phi_2)e^{-i\omega t}. \tag{7}$$

These displacement potentials each satysfy a scalar Helmholtz equation (3) as before with k_i, K, σ_i, ψ, α, β, ω_0, and κ also the same as in the previous section.

In cylindrical co-ordinates, the plate stresses defined in terms of three-dimensional stress theory are given by

$$(N_{rr}, N_{\theta\theta}, N_{zz}, N_{r\theta}) = \int_{-h}^{h} (\sigma_{rr}, \sigma_{\theta\theta}, \sigma_{zz}, \sigma_{r\theta})\, \mathrm{d}z,$$
$$(R_{rz}, R_{\theta z}) = \int_{-h}^{h} (\sigma_{rz}, \sigma_{\theta z}) z\, \mathrm{d}z. \tag{8}$$

For the geometry of this problem one need only be concerned with N_{rr}, $N_{r\theta}$ and R_{rz}. The necessary plate stresses are given by

$$N_{rr} = 2h[(\lambda + 2\mu)\partial v_r/\partial r + \lambda((1/r)\partial v_\theta/\partial\theta + v_r/r + v_z/h)],$$
$$N_{r\theta} = 2h\mu((1/r)\partial v_r/\partial\theta + \partial v_\theta/\partial r - v_\theta/r), \quad R_{rz} = (2\mu h^2/3)\partial v_z/\partial r. \tag{9}$$

3.1. PLANE WAVES

Now the case of an incident plane $S0$ wave is considered. Suppressing $\mathrm{e}^{-\mathrm{i}\omega t}$ throughout the following analysis one writes

$$\phi_1^{INC} = \mathrm{e}^{\mathrm{i}k_1 x} = \mathrm{e}^{\mathrm{i}k_1 r\cos\theta} = \sum_{n=-\infty}^{\infty} \mathrm{i}^n J_n(k_1 r)\mathrm{e}^{\mathrm{i}n\theta}, \quad \phi_2^{INC} = \Psi^{INC} = 0. \tag{10}$$

For a cylindrical scatterer at the origin of the co-ordinate system, the general solutions of the scattered and transmitted waves are expanded as

$$\phi_1^{SCAT} = \sum_{n=-\infty}^{\infty} A_n \mathrm{i}^n \mathrm{H}_n(k_1 r)\mathrm{e}^{\mathrm{i}n\theta}, \quad \phi_2^{SCAT} = \sum_{n=-\infty}^{\infty} B_n \mathrm{i}^n \mathrm{H}_n(k_2 r)\mathrm{e}^{\mathrm{i}n\theta},$$
$$\Psi^{SCAT} = \sum_{n=-\infty}^{\infty} C_n \mathrm{i}^n \mathrm{H}_n(Kr)\mathrm{e}^{\mathrm{i}n\theta}, \quad \phi_1^{TRANS} = \sum_{n=-\infty}^{\infty} A'_n \mathrm{i}^n \mathrm{J}_n(k'_1 r)\mathrm{e}^{\mathrm{i}n\theta},$$
$$\phi_2^{TRANS} = \sum_{n=-\infty}^{\infty} B'_n \mathrm{i}^n \mathrm{J}_n(k'_2 r)\mathrm{e}^{\mathrm{i}n\theta}, \quad \Psi^{TRANS} = \sum_{n=-\infty}^{\infty} C'_n \mathrm{i}^n \mathrm{J}_n(K' r)\mathrm{e}^{\mathrm{i}n\theta}, \tag{11}$$

where $A_n, \ldots, C'_n$ are unknown modal coefficients to be determined from the boundary conditions, $\mathrm{J}_n(\cdot)$ are Bessel functions and $\mathrm{H}_n(\cdot)$ are Hankel functions of the first kind. The Bessel and Hankel functions have been chosen so that the transmitted waves are finite at the origin and the scattered waves take the form of outgoing cylindrical waves at infinity.

The boundary conditions for welded contact are continuity of displacements at $r = a$

$$v_r^{INC} + v_r^{SCAT} = v_r^{TRANS}, \quad v_\theta^{INC} + v_\theta^{SCAT} = v_\theta^{TRANS}, \quad v_z^{INC} + v_z^{SCAT} = v_z^{TRANS}, \tag{12}$$

and continuity of plate stresses at $r = a$,

$$N_{rr}^{INC} + N_{rr}^{SCAT} = N_{rr}^{TRANS}, \quad N_{r\theta}^{INC} + N_{r\theta}^{SCAT} = N_{r\theta}^{TRANS}, \quad R_{rz}^{INC} + R_{rz}^{SCAT} = R_{rz}^{TRANS}. \tag{13}$$

These six equations in six unknowns can be written as

$$\begin{pmatrix} (k_1a)\mathrm{H}_n'(k_1a) & (k_2a)\mathrm{H}_n'(k_2a) & (\mathrm{i}n)\mathrm{H}_n(Ka) & -(k_1'a)\mathrm{J}_n'(k_1'a) & -(k_2'a)\mathrm{J}_n'(k_2'a) & -(\mathrm{i}n)\mathrm{J}_n(K'a) \\ (\mathrm{i}n)\mathrm{H}_n(k_1a) & (\mathrm{i}n)\mathrm{H}_n(k_2a) & -(Ka)\mathrm{H}_n'(Ka) & -(\mathrm{i}n)\mathrm{J}_n(k_1'a) & -(\mathrm{i}n)\mathrm{J}_n(k_2'a) & (K'a)\mathrm{J}_n'(K'a) \\ (\sigma_1a^2/h)\mathrm{H}_n(k_1a) & (\sigma_2a^2/h)\mathrm{H}_n(k_2a) & 0 & -((h'/h)\sigma_1'a^2/h')\mathrm{J}_n(k_1'a) & -((h'/h\sigma_2'a^2/h')\mathrm{J}_n(k_2'a) & 0 \\ B_{41} & B_{42} & B_{43} & B_{44} & B_{45} & B_{46} \\ B_{51} & B_{52} & B_{53} & B_{54} & B_{55} & B_{56} \\ B_{61} & B_{62} & 0 & B_{64} & B_{65} & 0 \end{pmatrix}$$

$$\times \begin{pmatrix} A_n \\ B_n \\ C_n \\ A_n' \\ B_n' \\ C_n' \end{pmatrix} = \begin{pmatrix} -(k_1a)\mathrm{J}_n'(k_1a) \\ -(\mathrm{i}n)\mathrm{J}_n(k_1a) \\ -(\sigma_1a^2/h)\mathrm{J}_n(k_1a) \\ C_{41} \\ C_{51} \\ C_{61} \end{pmatrix}, \tag{14}$$

where

$$\alpha_{1,2} = \tfrac{1}{2}(c_L^2/c_T^2)(\sigma_{1,2}a^2/h - (k_{1,2}a)^2) + n^2 - \sigma_{1,2}a^2/h,$$

$$\alpha_{1,2}' = \tfrac{1}{2}(c_L'^2/c_T'^2)(\sigma_{1,2}'a^2/h' - (k_{1,2}'a)^2) + n^2 - \sigma_{1,2}'a^2/h'$$

and the prime on the Bessel and Hankel functions denotes differentiation with respect to argument.

Note also the definitions

$$
\begin{aligned}
B_{41} &= [\alpha_1 \mathrm{H}_n(k_1 a) - (k_1 a)\mathrm{H}'_n(k_1 a)],\\
B_{42} &= [\alpha_2 \mathrm{H}_n(k_2 a) - (k_2 a)\mathrm{H}'_n(k_2 a)],\\
B_{43} &= [(\mathrm{i}nKa)\mathrm{H}'_n(Ka) - (\mathrm{i}n)\mathrm{H}_n(Ka)],\\
B_{44} &= -(\mu'/\mu)(h'/h)[\alpha'_1 \mathrm{J}_n(k'_1 a) - (k'_1 a)\mathrm{J}'_n(k'_1 a)],\\
B_{45} &= -(\mu'/\mu)(h'/h)[\alpha'_2 \mathrm{J}_n(k'_2 a) - (k'_2 a)\mathrm{J}'_n(k'_2 a)],\\
B_{46} &= -(\mu'/\mu)(h'/h)[(\mathrm{i}nK'a)\mathrm{J}'_n(K'a) - (\mathrm{i}n)\mathrm{J}_n(K'a)],
\end{aligned}
\tag{15}
$$

$$
\begin{aligned}
B_{51} &= [(2\mathrm{i}nk_1 a)\mathrm{H}'_n(k_1 a) - (2\mathrm{i}n)\mathrm{H}_n(k_1 a)],\\
B_{52} &= [(2\mathrm{i}nk_2 a)\mathrm{H}'_n(k_2 a) - (2\mathrm{i}n)\mathrm{H}_n(k_2 a)],\\
B_{53} &= [((Ka)^2 - 2n^2)\mathrm{H}_n(Ka) - (2Ka)\mathrm{H}'_n(Ka)],\\
B_{54} &= -(\mu'/\mu)(h'/h)[(2\mathrm{i}nk'_1 a)\mathrm{J}'_n(k'_1 a) - (2\mathrm{i}n)\mathrm{J}_n(k'_1 a)],\\
B_{55} &= -(\mu'/\mu)(h'/h)[(2\mathrm{i}nk'_2 a)\mathrm{J}'_n(k'_2 a) - (2\mathrm{i}n)\mathrm{J}_n(k'_2 a)],\\
B_{56} &= -(\mu'/\mu)(h'/h)[((K'a)^2 - 2n^2)\mathrm{J}_n(K'a) + (2K'a)\mathrm{J}'_n(K'a)],
\end{aligned}
\tag{16}
$$

$$
\begin{aligned}
B_{61} &= [(\sigma_1 a^2/h)(k_1 a)\mathrm{H}'_n(k_1 a)], \quad B_{62} = [(\sigma_2 a^2/h)(k_2 a)\mathrm{H}'_n(k_2 a)],\\
B_{64} &= -(\mu'/\mu)(h'/h)^3[(\sigma'_1 a^2/h')(k'_1 a)\mathrm{J}'_n(k'_1 a)],\\
B_{65} &= -(\mu'/\mu)(h'/h)^3[(\sigma'_2 a^2/h')(k'_1 a)\mathrm{J}'_n(k'_2 a)],
\end{aligned}
\tag{17}
$$

$$
\begin{aligned}
C_{41} &= -[\alpha_1 \mathrm{J}_n(k_1 a) - (k_1 a)\mathrm{J}'_n(k_1 a)],\\
C_{51} &= -[(2\mathrm{i}nk_1 a)\mathrm{J}'_n(k_1 a) - (2\mathrm{i}n)\mathrm{J}_n(k_1 a)],\\
C_{61} &= -[(\sigma_1 a^2/h)(k_1 a)\mathrm{J}'_n(k_1 a)].
\end{aligned}
\tag{18}
$$

One can solve this matrix equation for the unknown modal coefficents

$$
\begin{aligned}
A_n &= \Delta_1/\Delta_0, \quad B_n = \Delta_2/\Delta_0, \quad C_n = \Delta_3/\Delta_0,\\
A'_n &= \Delta_4/\Delta_0, \quad B'_n = \Delta_5/\Delta_0, \quad C'_n = \Delta_6/\Delta_0,
\end{aligned}
\tag{19}
$$

where Δ_0–Δ_6 are the Cramer's rule determinants.

One now can write explicit expressions for the modal coefficients for the case of a plane wave incident upon a general cylindrical scatterer. However, in order to explain the scattering effects seen in Figure 1, the specific case of the cylindrical scatterer being a through hole will be considered. In this case, the normal tractions at the boundary must equal zero, and one sets $A'_n \equiv B'_n \equiv C'_n \equiv 0$. Now one has three unknown modal coefficients (A_n, B_n, C_n). Therefore, only the three plate stress boundary conditions of equation (13) are considered. For this case, the matrix equation becomes

$$\begin{pmatrix} B_{41} & B_{42} & B_{43} \\ B_{51} & B_{52} & B_{53} \\ B_{61} & B_{62} & 0 \end{pmatrix} \begin{pmatrix} A_n \\ B_n \\ C_n \end{pmatrix} = \begin{pmatrix} C_{41} \\ C_{51} \\ C_{61} \end{pmatrix}, \tag{20}$$

where the B_{ij}'s and C_{ij}'s are as defined in equations (15–18). Again applying Cramer's rule the Δ's are now easily expanded to give

$$\begin{aligned} \Delta_0 = {} & (\sigma_1 a^2/h)(k_1 a)(\alpha_2 (Ka)^2 + 2n^2(1-\alpha_2))\mathrm{H}_n'(k_1 a)\mathrm{H}_n(k_2 a)\mathrm{H}_n(Ka) \\ & + 2(\sigma_1 a^2/h)(k_1 a)(Ka)(\alpha_2 - n^2)\mathrm{H}_n'(k_1 a)\mathrm{H}_n(k_2 a)\mathrm{H}_n'(Ka) \\ & + (k_1 a)(k_2 a)(Ka)^2(\sigma_2 a^2/h - \sigma_1 a^2/h)\mathrm{H}_n'(k_1 a)\mathrm{H}_n'(k_2 a)\mathrm{H}_n(Ka) \\ & - 2(k_1 a)(k_2 a)(Ka)(n^2-1)(\sigma_2 a^2/h - \sigma_1 a^2/h)\mathrm{H}_n'(k_1 a)\mathrm{H}_n'(k_2 a)\mathrm{H}_n'(Ka) \\ & - (\sigma_2 a^2/h)(k_2 a)(\alpha_1 (Ka)^2 + 2n^2(1-\alpha_1))\mathrm{H}_n(k_1 a)\mathrm{H}_n'(k_2 a)\mathrm{H}_n(Ka) \\ & - 2(\sigma_2 a^2/h)(k_2 a)(Ka)(\alpha_1 - n^2)\mathrm{H}_n(k_1 a)\mathrm{H}_n'(k_2 a)\mathrm{H}_n'(Ka), \end{aligned} \tag{21}$$

$$\begin{aligned} \Delta_1 = {} & -(\sigma_1 a^2/h)(k_1 a)(\alpha_2 (Ka)^2 + 2n^2(1-\alpha_2))\mathrm{J}_n'(k_1 a)\mathrm{H}_n(k_2 a)\mathrm{H}_n(Ka) \\ & - 2(\sigma_1 a^2/h)(k_1 a)(Ka)(\alpha_2 - n^2)\mathrm{J}_n'(k_1 a)\mathrm{H}_n(k_2 a)\mathrm{H}_n'(Ka) \\ & - (k_1 a)(k_2 a)(Ka)^2(\sigma_2 a^2/h - \sigma_1 a^2/h)\mathrm{J}_n'(k_1 a)\mathrm{H}_n'(k_2 a)\mathrm{H}_n(Ka) \\ & + 2(k_1 a)(k_2 a)(Ka)(n^2-1)(\sigma_2 a^2/h - \sigma_1 a^2/h)\mathrm{J}_n'(k_1 a)\mathrm{H}_n'(k_2 a)\mathrm{H}_n'(Ka) \\ & + (\sigma_2 a^2/h)(k_2 a)(\alpha_1 (Ka)^2 + 2n^2(1-\alpha_1))\mathrm{J}_n(k_1 a)\mathrm{H}_n'(k_2 a)\mathrm{H}_n(Ka) \\ & + 2(\sigma_2 a^2/h)(k_2 a)(Ka)(\alpha_1 - n^2)\mathrm{J}_n(k_1 a)\mathrm{H}_n'(k_2 a)\mathrm{H}_n'(Ka), \end{aligned} \tag{22}$$

$$\Delta_2 = -2\mathrm{i}/\pi \left(\frac{\sigma_1 a^2}{h}\right)[(\alpha_1 (Ka)^2 + 2n^2(1-\alpha_1))\mathrm{H}_n(Ka) - 2(Ka)(\alpha_1 - n^2)\mathrm{H}_n'(Ka)], \tag{23}$$

$$\Delta_3 = \frac{4n}{\pi}\left[(k_2 a)\left(\frac{\sigma_2 a^2}{h} - \frac{\sigma_1 a^2}{h}\right)(\alpha_1 - 1)\mathrm{H}_n'(k_2 a) - \left(\frac{\sigma_1 a^2}{h}\right)(\alpha_2 - \alpha_1)\mathrm{H}_n(k_2 a)\right]. \tag{24}$$

The behavior of the $S0$ Lamb wave field for the case of a plane wave incident upon a hole can now be examined using the equations for ϕ_1^{INC}, ϕ_1^{SCAT}, and A_n. The standard representation for scattering results predicted by theory is a polar plot of the magnitude of the amplitude of the scattered wave as a function of θ. Figure 3 shows this plane wave scattering amplitude for holes of radius $a = 0{\cdot}25 \times 10^{-2}$ m, $a = 0{\cdot}75 \times 10^{-2}$ m, and $a = 1{\cdot}27 \times 10^{-2}$ m. In order to match the experiments, the values $\lambda = 6{\cdot}293 \times 10^{10}$ kg/ms^2, $\mu = 2{\cdot}677 \times 10^{10}$ kg/ms^2, $\rho = 2700$ kg/m^3, $\omega = 2\pi(1{\cdot}1) \times 10^6$ Hz and $h = 1{\cdot}143 \times 10^{-3}$ m have been chosen. For the smallest hole (Figure 3(a)), the largest lobe is in the 180° direction and

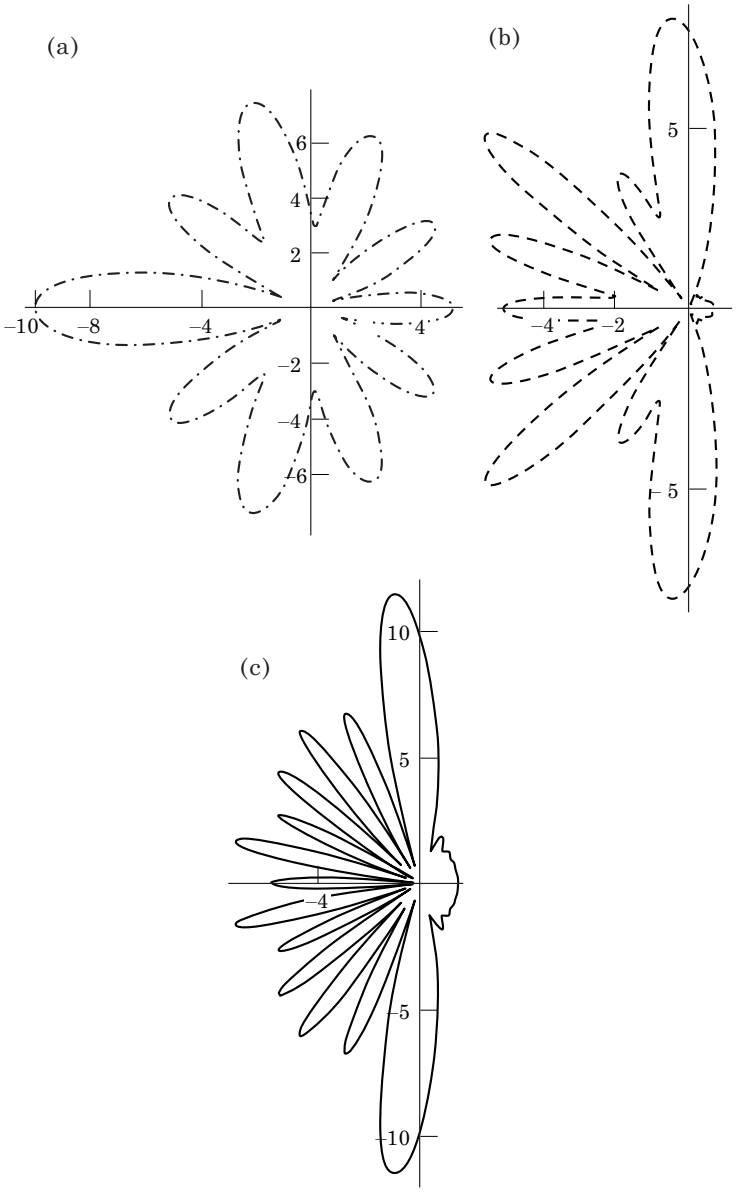

Figure 3. Polar plot of the magnitude of the scattered amplitude of a plane wave incident from the left upon a hole with radii: (a) $a = 0{\cdot}25 \times 10^{-2}$ m; (b) $a = 0{\cdot}75 \times 10^{-2}$ m and (c) $a = 1{\cdot}27 \times 10^{-2}$ m.

the other lobes are of approximately the same amplitude and are about evenly spaced over the remaining range of angles. For the middle hole (Figure 3(b)), the largest lobes are near 90° and 270°, there is only a small forward scattered component, and the remaining lobes are all in the backscattered direction. Finally for the largest hole (Figure 3(c)), the largest lobes are still near the 90° and 270° directions, there are more lobes in the backscattered direction, and there is still a small forward scattered component.

3.2. POINT SOURCE AND FINITE SOURCE

The case of the incident $S0$ Lamb wave being generated by a point source at distance r_0 from the origin is next considered. The incident potential is written as

$$\phi_1^{INC} = \sum_{n=-\infty}^{\infty} (-1)^n \mathrm{H}_n(k_1 r_0)\mathrm{J}_n(k_1 r)\mathrm{e}^{\mathrm{i}n\theta}, \tag{25}$$

with the same general forms for the scattered and transmitted potentials. The boundary conditions for this problem are again given by equations (12) and (13), providing six equations for the six unknowns. By Cramer's rule the coefficients are

$$\begin{aligned} &A_n = \mathrm{H}_n(k_1 r_0)(\Delta_1/\Delta_0), \quad B_n = \mathrm{H}_n(k_1 r_0)(\Delta_2/\Delta_0), \quad C_n = \mathrm{H}_n(k_1 r_0)(\Delta_3/\Delta_0), \\ &A'_n = \mathrm{H}_n(k_1 r_0)(\Delta_4/\Delta_0), \quad B'_n = \mathrm{H}_n(k_1 r_0)(\Delta_5/\Delta_0), \quad C'_n = \mathrm{H}_n(k_1 r_0)(\Delta_6/\Delta_0), \end{aligned} \tag{26}$$

where the Δ's are the same as in the case of a plane wave incident on a general cylindrical scatterer so that the algebra does not have to be repeated. The behavior of the $S0$ Lamb wave field for the case of a point source can thus be examined using the equations for ϕ_1^{INC}, ϕ_1^{SCAT}, and A_n.

In the laboratory experiments one uses standard contact piezoelectric transducers to generate the Lamb waves in the plate. Although angle beam transducers are very efficient at generating particular Lamb wave modes via Snell's law, one finds that normal incident shear or longitudinal contact transducers effectively generate Lamb waves in thin plates [31–33]. They generate all possible modes with varying efficiencies so one typically limits the frequency–thickness range so that the higher-order modes are either fully cut off or at least highly attenuated. The transducers are, of course, finite sources which generate finite beams, so the plane wave and point source incident waves cannot be expected to accurately describe the Lamb wave propagation in the experiments. However, by Huygen's principle, one can model any finite source by a superposition of point sources.

The shear contact transducers used in the present parallel projection tomography (PPT) experiments generate a directional Lamb wave field which has been measured to be 100% at $\pm 0°$, 50% at $\pm 20°$, and 26% at $\pm 30°$. A good aproximation to this beam pattern has been found to be a line of five point sources at a distance r_0 from the center of the co-ordinate system as shown in Figure 4. For $|\vec{r}_0| = 8{\cdot}75$ cm, the point separation to simulate the measured beam pattern is $B = 0{\cdot}32$ cm, and the necessary relative amplitudes of the point sources are

$$C_j = 1{\cdot}0, \quad j = 1, 2, 4, 5, \quad C_3 = 3{\cdot}0. \tag{27}$$

In the experiments, the transducer pair starts at a position well above the flaw and scans down past the flaw to a position well below the flaw. Straightforward algebra now gives scattering expressions for each point source in terms of the known parameters $\vec{r}_0 = (|\vec{r}_0|, \theta)$ and B, and one can sum the individual

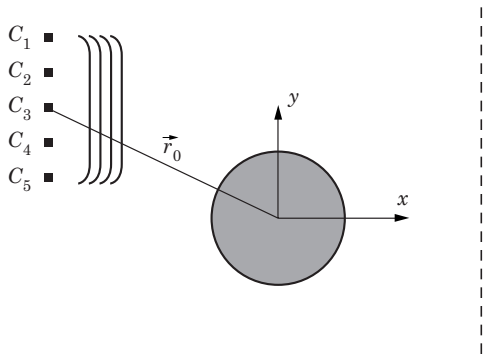

Figure 4. Geometry for the finite source scattering from the cylindrical inclusion in the plate. The five point sources C_1–C_5 separated from each other by a distance B are shown, with the amplitude of the middle point source C_3 chosen as three times the others to generate a finite beam propagating in the x direction. The through hole is at the origin of the co-ordinate system, and the vertical dashed line to the right shows where the resulting place displacements are calculated.

contributions of the point sources to obtain the scattered field for the finite source.

Figure 5 shows the magnitude of the scattered amplitude when the finite source has been shifted by $+3{\cdot}0 \times 10^{-2}$ m. For the small hole (Figure 5(a)), the scattering pattern looks quite different from the plane wave case. The largest lobes are still in the backscattered area, but they have been shifted to match the new position of the source. Also, instead of many separate lobes, combined lobes are seen. The results for the middle hole (Figure 5(b)) give a rotated version of those seen for the plane wave case. There is still the small forward scattered component, but it is joined by a small lobe. Also, combined lobes are again seen in the backscattered region. For the largest hole (Figure 5(c)), the results are essentially just a rotated version of those seen in the plane wave case with the addition of a large combined lobe and slight variations in the magnitudes of the lobes. One notes that in the plane wave and point source cases the incident wave interacts fully with the holes, large or small. However, the finite beam scatters differently from the holes depending on the offset and hole diameter.

Figure 6 shows the magnitude of the scattered amplitude when the finite source has been shifted by $+5{\cdot}0 \times 10^{-2}$ m. For the small hole (Figure 6(a)), the scattering pattern looks quite different from the plane wave and $+3$ shift cases. Only two large lobes are seen in the backscattered direction, and three smaller lobes are seen in the forward direction. For the middle hole (Figure 6(b)), the results are again a rotated version of those seen previously. However, the magnitude of the backscattered lobes has increased, while that of the other lobes has decreased. Also note that the extra lobe in the forward direction has increased in magnitude. For the large hole (Figure 6(c)), the pattern is again rotated. The magnitude of the backscattered lobes has increased slightly from the $+3$ shift cases while that of the others has decreased slightly. There are some additional combined lobes, one of the backscattered lobes has gotten much smaller, and an additional forward scattered lobe has appeared.

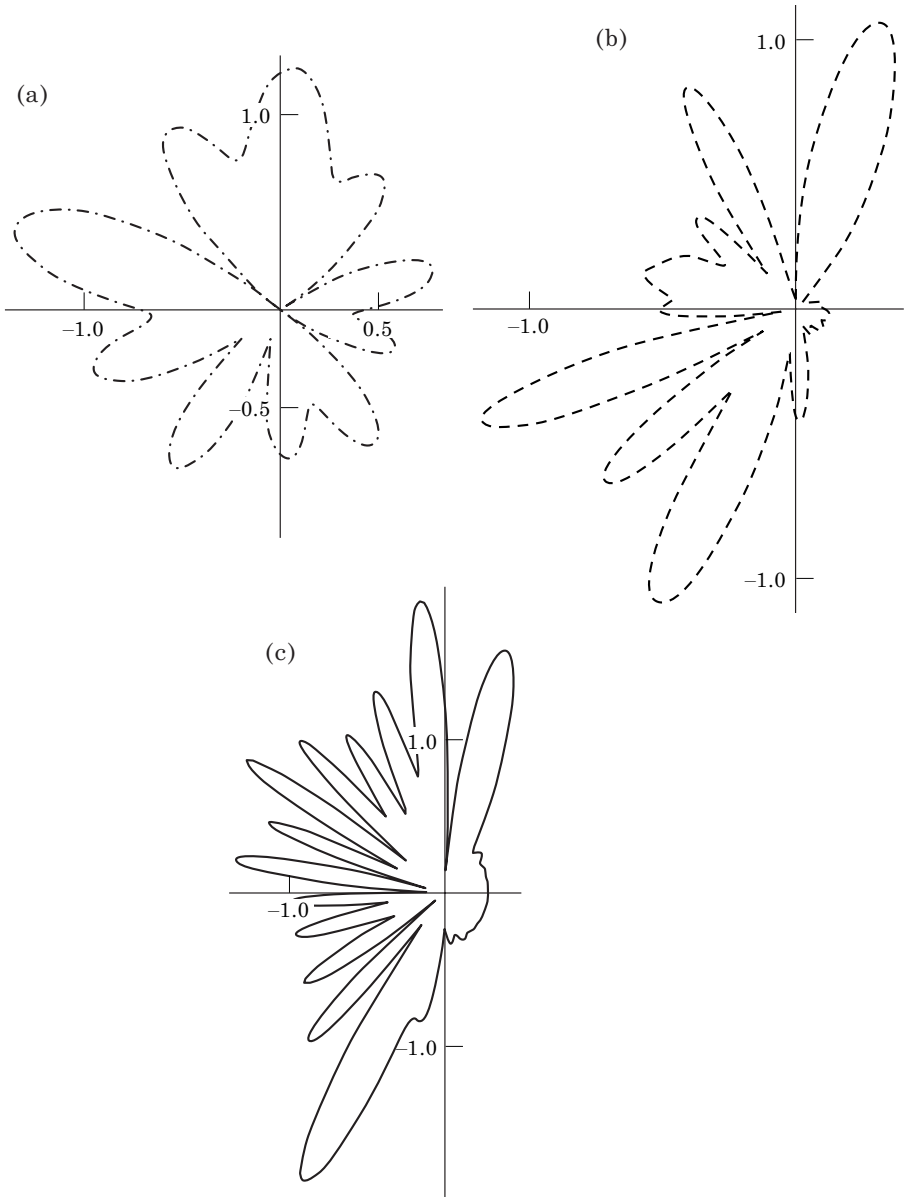

Figure 5. Polar plot of the magnitude of the scattered amplitude of a finite source wave incident from the left upon a hole with radii: (a) $a = 0{\cdot}25 \times 10^{-2}$ m; (b) $a = 0{\cdot}75 \times 10^{-2}$ m and (c) $a = 1{\cdot}27 \times 10^{-2}$ m, when the source has been shifted by $+3$ cm in the y direction.

4. SIMULATION OF PLATE DISPLACEMENTS

Although, some differences in the scattering patterns have been noted for the finite source case as the hole size increases, such as the existence of the forward scattering components and changes in the lobe structure, these differences do not obviously cause the scattering effects seen in the tomographic images of the large hole, and one concludes plotting the magnitude of the scattered amplitude as a function of θ is not the optimum way to present the results. It assumes far-field

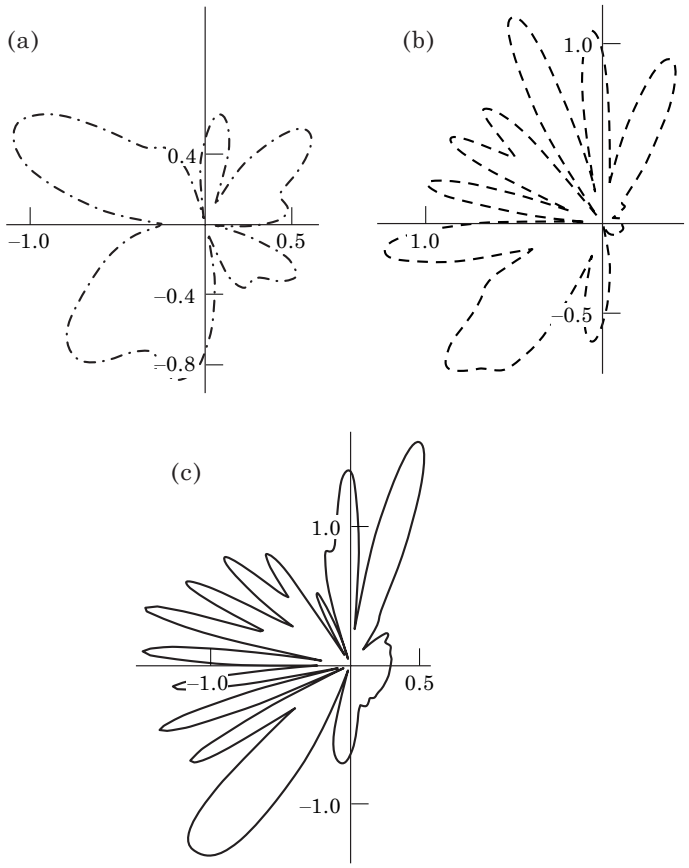

Figure 6. Polar plot of the magnitude of the scattered amplitude of a finite source wave incident from the left upon a hole with radii: (a) $a = 0{\cdot}25 \times 10^{-2}$ m; (b) $a = 0{\cdot}75 \times 10^{-2}$ m and (c) $a = 1{\cdot}27 \times 10^{-2}$ m, when the source has been shifted by $+5$ cm in the y direction.

and neglects physics that may be important here. Instead the values actually registered by the receiving transducers in the experiments will be simulated.

In the present experiments one uses a piezoelectric transducer to receive the Lamb waves. The vibrations of the surface of the plate cause the piezoelectric element to vibrate, and this generates the received electric signal corresponding to the Lamb waves. Therefore, instead of the scattered amplitude as defined above, one needs to examine the full motion of the top surface of the plate. In addition, the transducer is receiving the incident wave as well as the scattered wave, so both of these contributions need to be considered in our calculations.

In the experiments, the Lamb waves are generated at one location and received at a separate location. For PPT, the transducers are moved together as a pair, and for a given scan, the generating and receiving locations can be represented by $(-x, y)$ and (x, y) respectively. As the scan progresses, the x-co-ordinate of the receiver location remains fixed, while the y-co-ordinate varies. Thus, one obtains data along a line parallel to the y-axis.

The vertical displacement of the combined incident and scattered $S0$ waves can be calculated at each receiver location. Also, since the transducer is only

sensitive to the real motion of the plate, only the real part of the vertical displacement is used. These calculated vertical displacement values can then be plotted as a function of y to form vertical displacement curves. These curves represent the vertical displacement of the top surface of the plate along a specified line, x = constant, as shown in Figure 4.

Figure 7 shows the vertical displacement curves for the case of a plane $S0$ wave incident upon holes of radius $a = 0{\cdot}25 \times 10^{-2}$ m, $a = 0{\cdot}75 \times 10^{-2}$ m,

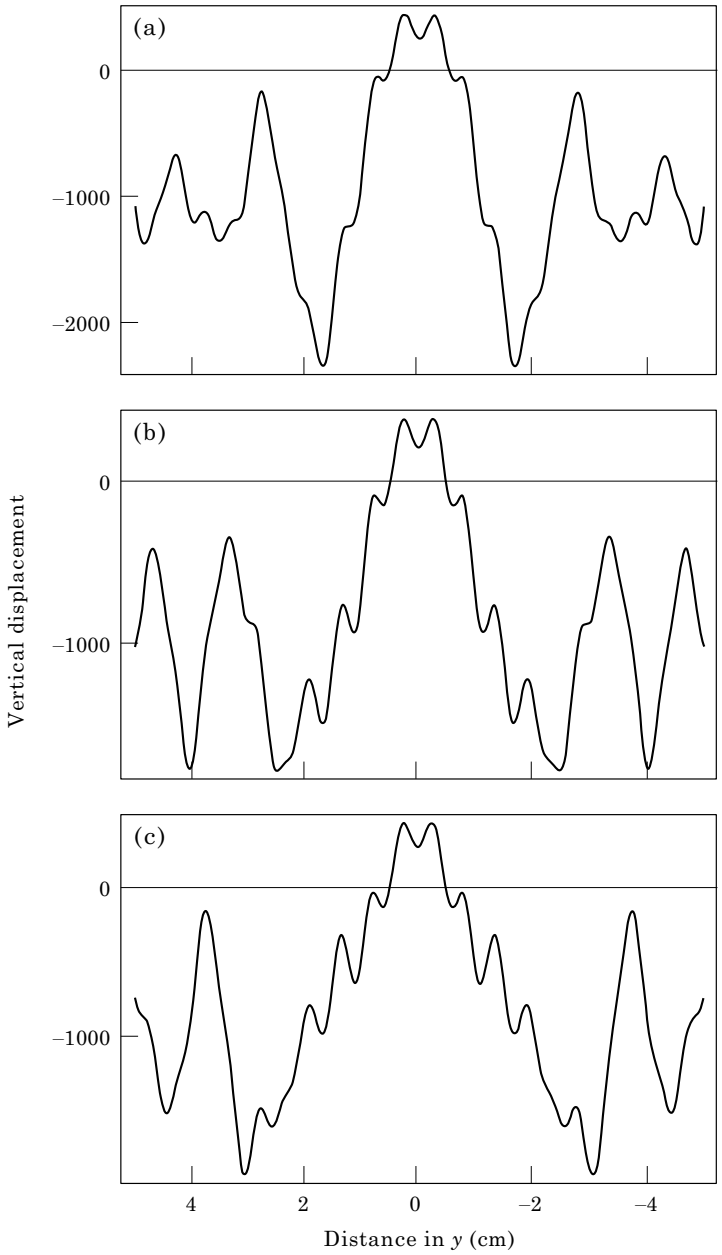

Figure 7. Vertical displacement curve for the case of a plane wave incident from the left upon a hole with radii: (a) $a = 0{\cdot}25 \times 10^{-2}$ m; (b) $a = 0{\cdot}75 \times 10^{-2}$ m and (c) $a = 1{\cdot}27 \times 10^{-2}$ m.

and $a = 1{\cdot}27 \times 10^{-2}$ m. In order to match the experiments, the values $\lambda = 6{\cdot}293 \times 10^{10}$ kg/ms^2, $\mu = 2{\cdot}677 \times 10^{10}$ kg/ms^2, $\rho = 2700$ kg/m^3, $\omega = 2\pi(1{\cdot}1) \times 10^6$ Hz, and $h = 1{\cdot}143 \times 10^{-3}$ m have again been chosen, and the x-co-ordinate of the receiver line is set as $8{\cdot}75 \times 10^{-2}$ m. In the absence of scattering, one would simply expect to see a uniform value for the vertical displacement except in the flaw area where one would expect a shadow region since the $S0$ Lamb wave cannot propagate through the hole. Instead, one sees fluctuations in the magnitude of the vertical displacement throughout the curve. These variations are due to the scattering of the plane wave from the hole. Comparing the three figures, one sees that the majority of the curve is negative indicating motion of the plate below $z = h$. However, in the flaw region about $y = 0$, the vertical displacement is positive indicating motion above $z = h$. The main difference between the curves as the hole size increases is that the maximum negative peaks move farther away from $y = 0$ and their magnitude decreases. However, there are no sharp changes in the curves for the largest hole, and so nothing to indicate the scattering effects is seen in the tomographic images.

Figure 8 shows the vertical displacement curves for the case of a point source $S0$ wave incident upon holes of radius $a = 0{\cdot}25 \times 10^{-2}$ m, $a = 0{\cdot}75 \times 10^{-2}$ m, and $a = 1{\cdot}27 \times 10^{-2}$ m respectively. The values of λ, μ, ρ, ω, h, and of the x-co-ordinate of the receiver line are the same as above. In addition, the x-co-ordinate of the point source is set as $-8{\cdot}75 \times 10^{-2}$ m. Since the incident wave is cylindrical, the vertical displacement values along a line will not show if the magnitude of the vertical displacement is uniform. Instead one focuses on the flaw region. For the small hole (Figure 8(a)), the vertical displacement is negative in the flaw region until $y = \pm 1$ where it switches to a positive value until $y = \pm 2$. Over this region, the magnitude of the vertical displacement is decreasing. For the middle hole (Figure 8(b)), the vertical displacement remains negative out past $y = \pm 2$ and the magnitude is relatively constant other than for small oscillations. Finally for the large hole (Figure 8(c)), the vertical displacement is positive out to about $y = \pm 1{\cdot}3$ where it becomes negative. The magnitude in this region gradually decreases until $y = \pm 1{\cdot}3$ when it starts increasing again. This change in phase of the vertical displacement in the flaw region as the hole size increases could indicate the scattering effects seen in the tomographic images. It predicts a change in the motion of the plate, not just a change in the amplitude of the motion. However, the phase change is gradual for the point source case in which the incident wave still extends far past the flaw region.

Figure 9 shows the vertical displacement curves for the case of a finite source $S0$ wave incident upon holes of radius $a = 0{\cdot}25 \times 10^{-2}$ m, $a = 0{\cdot}75 \times 10^{-2}$ m, and $a = 1{\cdot}27 \times 10^{-2}$ m respectively. The values of λ, μ, ρ, ω, h, and of the x-co-ordinate of the receiver line are the same as above. In addition, the x-co-ordinate of the point sources in the finite source is set as $-8{\cdot}75 \times 10^{-2}$ m. In all three plots, one sees that the magnitude is basically the same until one approaches the edge of the hole. At this point the magnitude dramatically increases due to the large contribution of the scattered field with the incident field at the receiver location, and one has a large positive vertical displacement. Next, one considers the flaw region. For the small and medium holes (Figures 9(a) and (b)), the

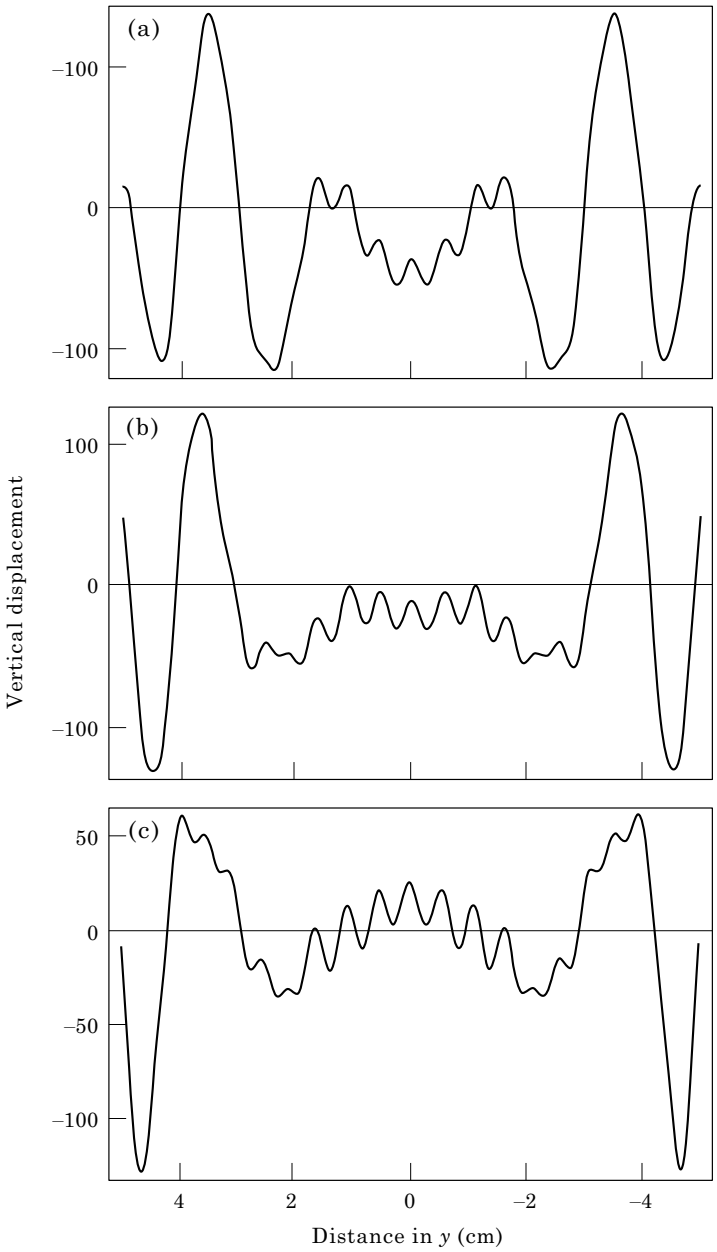

Figure 8. Vertical displacement curve for the case of a point source wave incident from the left upon a hole with radii: (a) $a = 0{\cdot}25 \times 10^{-2}$ m; (b) $a = 0{\cdot}75 \times 10^{-2}$ m and (c) $a = 1{\cdot}27 \times 10^{-2}$ m.

magnitude drops to almost zero at the edge of the hole, where the vertical displacement becomes negative, and then increases until $y = 0$. For the large hole (Figure 9(c)), the magnitude again decreases until the very edge of the hole, where the curve starts to oscillate between positive and negative vertical displacement values until $y = 0{\cdot}25$ where the magnitude increases and the vertical displacement remains positive until $y = 0$. While the large magnitudes

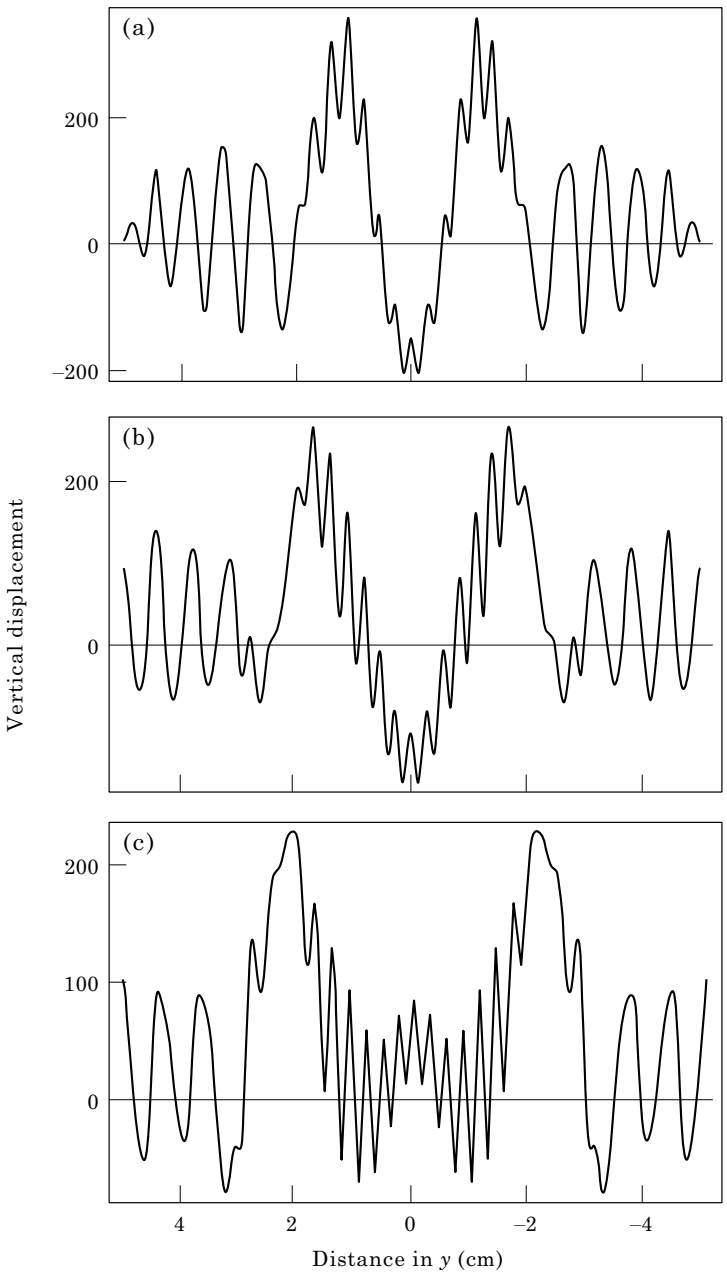

Figure 9. Vertical displacement curve for the case of a finite source wave incident from the left upon a hole with radii: (a) $a = 0{\cdot}25 \times 10^{-2}$ m; (b) $a = 0{\cdot}75 \times 10^{-2}$ m and (c) $a = 1{\cdot}27 \times 10^{-2}$ m.

near the edges of the holes indicate scattering effects, the rapid oscillations and positive vertical displacement values in the flaw region of the large hole indicate some additional effects. In contrast to the motion for the two smaller holes, the motion of the plate with the large hole rapidly oscillates between positive and negative values at the edge and just inside the flaw region. Then the plate settles into a positive vertical displacement at the center of the flaw region in contrast

to the negative vertical displacement seen for the two smaller holes. The rapid oscillations, which are over an area smaller than the transducer element size, could be responsible for the streaking effects seen in the tomographic images, while the phase change at the center of the flaw region may be responsible for the scalloping or other effects.

5. DISCUSSION

Isolated through holes in plates scatter Lamb waves, giving artifacts in tomographic reconstructions that have assumed straight, non-diffracting rays. Modelling this phenomenon is problematic because Lamb waves are guided waves which cannot be treated via standard scattering analysis. The Mindlin extensional wave plate theory provides a tractable framework, which still captures the important physical effects in our Lamb wave contact scanning measurements. By considering in some detail the scattering of $S0$ Lamb waves from isolated through holes with this theory, one has been able to explore the scattering behavior for various sizes of holes. The "point source" solution has been used to synthesize the total displacement fields of realistic $S0$ beams incident on holes of various sizes in order to confirm that scattering is important when the hole size is larger than the beam size. This correlates with the experimental results in which the starburst streaking pattern and scalloping were seen in a parallel projection tomography image for a large hole in the aluminum plate. This theory and the general scattering solution outlined here are also vital for the development of Lamb wave diffraction tomography, which is necessary to perform accurate reconstructions in the presence of strong scatterers.

REFERENCES

1. H. LAMB 1917 *Proceedings of the Royal Society of London* **XCIII**, 114–128. On waves in an elastic plate.
2. D. C. WORLTON 1961 *Journal of Applied Physics* **32**, 967–971. Experimental confirmation of Lamb waves at megacycle frequencies.
3. J. D. ACHENBACH 1973 *Wave Propagation in Elastic Solids*. New York: North-Holland.
4. J. A. HUDSON 1980 *The Excitation and Propagation of Elastic Waves*. Cambridge: Cambridge University Press.
5. L. M. BREKHOVSKIKH 1960 *Waves in Layered Media*. New York: Academic Press.
6. J. MIKLOWITZ 1978 *Elastic Waves and Waveguides*. New York: North-Holland.
7. K. F. GRAFF 1980 *Wave Motion in Elastic Solids*. New York: Dover.
8. H. KOLSKY 1963 *Stress Waves in Solids*. New York: Dover.
9. B. A. AULD 1990 *Acoustic Fields and Waves in Solids*, second edition. Malabar, FL: Robert E. Krieger.
10 W. WRIGHT, D. HUTCHINS, D. JANSEN, D. SCHINDEL 1997 *IEEE Transactions of Ultrasonics, Ferroelectrics, and Frequency Control* **44**, 53–59. Air-coupled Lamb wave tomography.
11. D. P. JANSEN, D. A. HUTCHINS and J. T. MOTTRAM 1994 *Ultrasonics* **32**, 83–89. Lamb wave tomography of advanced composite laminates containing damage.
12. D. A. HUTCHINS, D. P. JANSEN and C. EDWARDS 1993 *Ultrasonics* **31**, 97–103. Lamb wave tomography using non-contact transduction.

13. D. P. JANSEN and D. A. HUTCHINS 1992 *Ultrasonics* **30**, 245–254. Immersion tomography using Rayleigh and Lamb waves.
14. D. P. JANSEN and D. A. HUTCHINS 1990 *IEEE Ultrasonics Symposium*, 1017–1020. Lamb wave tomography.
15. Y. NAGATA, J. HUANG, J. D. ACHENBACH and S. KRISHNASWAMY 1995 in *Review of Progress in Quantitative Nondestructive Evaluation* (D. O. Thompson and D. E. Chimenti, editors) **14**, 561–568. New York: Plenum Press: Lamb wave tomography using laser-based ultrasonics.
16. F. L. DEGERTEKIN, J. PEI, B. T. KHURI-YAKUB and K. C. SARASWAT 1994 *Applied Physics Letters* **64**, 1338–1340. *In-situ* acoustic temperature tomography of semiconductor wafers.
17. J. C. P. MCKEON 1998 *Department of Applied Science Doctoral Dissertation: the college of William and Mary in Virginia*. Tomography applied to Lamb wave contact scanning nondestructive evaluation.
18. J. C. P. MCKEON and M. K. HINDERS 1999 in *Review of Progress in Quantitative Nondestructive Evaluation*, (D. O. Thompson and D. E. Chimenti, editors) **18** New York: Plenum Press: Lamb wave tomographic imaging system.
19. M. K. HINDERS, E. V. MALYARENKO and J. C. P. MCKEON 1999 in *Nondestructive Evaluation of Aging Aircraft, Airports, and Aerospace Hardware III* (A. K. Mal, editor). *Proceedings of SPIE* **3586**, 279–291. Ultrasonic Lamb wave tomographic scanning.
20. L. WANG and J. SHEN 1997 *Ultrasonics* **35**, 451–457. Scattering of elastic waves by a crack in a isotropic plate.
21. T. K. KAPOOR and H. SCHMIDT 1997 *Journal of the Acoustical Society of America* **102**, 256–265. Acoustic scattering from a three-dimensional proturbance on a thin, infinite, submerged elastic plate.
22. A. N. NORRIS and C. VEMULA 1995 *Journal of Sound and Vibration* **181**, 115–125. Scattering of flexural waves on thin plates.
23. A. SAFAEINILI and R. A. ROBERTS 1995 in *Review of Progress in Quantitative Nondestructive Evaluation* (D. O. Thompson and D. E. Chimenti, editors) **14**, 147–154. New York: Plenum Press. An efficient approximate model for elastic wave scattering in plates.
24. S. W. LIU, S. K. DATTA and A. H. SHAH 1992 in *Review of Progress in Quantitative Nondestructive Evaluation* (D. O. Thompson and D. E. Chimenti, editors) **11**, 73–80. New York: Plenum Press. Transient scattering of Rayleigh–Lamb waves by surface-breaking and buried cracks in a plate.
25. G. S. VERDICT, P. H. GIEN and C. P. BURGER 1992 in *Review of Progress in Quantitative Nondestructive Evaluation* (D. O. Thompson and D. E. Chimenti, editors) **11**, 97–104. New York: Plenum Press. Finite element study of Lamb wave interactions with holes and through thickness defects in thin metal plates.
26. T. R. KANE and R. D. MINDLIN 1956 *Journal of Applied Mechanics* **78**, 277–283. High-frequency extensional vibrations of plates.
27. T. R. KANE 1957 *Journal of Applied Mechanics* **79**, 213-220. Reflection of dilatational waves at the edge of a plate.
28. R. D. MINDLIN and M. A. MEDICK 1959 *Journal of Applied Mechanics* **80**, 561–569. Extensional vibrations of elastic plates.
29. Y. H. PAO and C. C. MOW 1973 *Diffraction of Elastic Waves and Dynamic Stress Concentrations*. New York: Crane-Russak.
30. C. VEMULA and A. N. NORRIS 1997 *Wave Motion* **26**, 1–12. Flexural wave propagation and scattering on this plates using Mindlin theory.
31. J. KRAUTKRAMER and H. KRAUTKRAMER 1990 *Ultrasonic Testing of Materials*, fourth edition. New York: Springer-Verlag.
32. A. H. HARKER 1988 *Elastic Waves in Solids*. Philadelphia: Adam Hilger.
33. I. A. VICTOROV 1967 *Rayleigh and Lamb Waves*. New York: Plenum Press.